RSC Advances

PAPER

View Article Online
View Journal | View Issue



Cite this: *RSC Adv.*, 2024, **14**, 4285

# Fe-doped nanodiamond-based photo-Fenton catalyst for dual-modal fluorescence imaging and improved chemotherapeutic efficacy against tumor hypoxia

Rajakar Selvam, [a] Wrenit Gem Pearl, [a] Elena Perevedentseva,[ab] Artashes Karmenyan[a] and Chia-Liang Cheng *[a]

The deficiency of oxygen in most solid tumors plays a profound role in their proliferation, metastasis, and invasion and contributes to their resistance to treatments such as radiation, chemotherapy, and photodynamic therapy (PDT). A therapeutic approach based on the Fenton reaction has received considerable interest as a means of treating cancer with ROS-based nano catalytic medicine, referred to as chemodynamic therapy (CDT). A range of modified treatment strategies are being explored to enhance both CDT and conventional methods of therapy. These include Fenton-like reactions, photo-enhanced Fenton reactions, and Fenton catalytic-enhanced synergistic therapies. In this article, we propose and demonstrate a photochemotherapy (PCT) strategy for cancer treatment utilizing near-infrared (NIR)-induced Fenton reactions using Fe-doped nanodiamond (FeND). When FeND is exposed to human lung cancer cells A549, it exhibits outstanding biocompatibility. However, when particle-treated cells are exposed to NIR laser radiation, the particle exhibits cytotoxicity to a certain degree. The anticancer medication doxorubicin (DOX) was adsorbed onto the FeND to address this issue. The conjugated DOX could undergo a redox cycle to generate excess $H_2O_2$ inside the cells, and in addition, DOX can also cause tumor cell apoptosis. Combining chemotherapy (*via* DOX) with a Fenton reaction results in enhanced therapeutic effectiveness. Moreover, the intrinsic fluorescence of the nanodiamond in FeND can be used to monitor the interaction of particles with cells as well as their localization, thus making it an excellent imaging probe. In our study, we found that FeND could serve as a CDT agent, biomarker, drug carrier, and potentially valuable candidate for CDT agents and contribute to the further development of more effective CDT platforms using nanodiamond.

Received 11th December 2023
Accepted 17th January 2024

DOI: 10.1039/d3ra08465e

rsc.li/rsc-advances



## 1. Introduction

Nanodiamond (ND) is a class of carbon material that emerged as a well-suited nanostructure for a wide range of biomedical applications, including drug delivery and bioimaging with superb biocompatibility.[1] ND has a unique all-carbon core–shell structure as the diamond's $sp^3$ carbon core is usually enclosed by the shells of $sp^2/sp^3$ carbons, making it different from other carbonaceous nanomaterials. Additionally, NDs feature a diverse array of surface functional groups, including carboxylic acids, esters, ethers, lactones, and amines, which can be functionalized depending on the intended application. Furthermore, the presence of optically active N–V centres in NDs provides stable fluorescence without photobleaching, making them ideal as bioimaging probes for cellular labelling and tracking purposes. In biological applications, NDs are widely utilized as bioimaging probes and are proposed as a carrier for chemotherapeutic drugs.[1,2] Chemotherapy is a widely used classic technique for treating cancer by exploiting the cytotoxic mechanism of drugs such as DOX. However, despite its advantages, the chemotherapeutic drugs are non-specific and might cause severe damage to the normal healthy cellular environment.

In recent years, PDT, a non-invasive technique to treat cancer by producing reactive oxygen species (ROS), has received a lot of interest. PDT uses a non-toxic dye molecule capable of transferring energy or electrons to other molecules in the surrounding environment when exposed to light of an appropriate wavelength to induce oxidative damage in cells, leading to apoptosis.[3] ROS are formed throughout the cell lifespan due to the partial reduction of molecular oxygen ($O_2$) in mitochondrial electron transport chains caused by aerobic respiration. A failure to maintain the balanced ratio between ROS generation and elimination would eventually lead to irreversible oxidative

[a]*Department of Physics, National Dong Hwa University, Taiwan. E-mail: clcheng@gms.ndhu.edu.tw*

[b]*P. N. Lebedev Institute of Physics, Russian Academy of Science, Moscow, Russia*

cellular damage, leading to apoptosis or necrosis.[4–6] PDT's efficiency is a function of $O_2$ and light penetration depth in the tumor microenvironment (TME). In the PDT process, molecular $O_2$ is a key component. Due to the aggressive proliferation of cancer cells and an insufficient supply of blood in the TME, the $O_2$ level in solid tumors is greatly reduced.[7] Furthermore, the endogenous biomolecules within the cells can absorb the irradiated light, resulting in a low penetration depth and giving rise to unsatisfactorily low therapeutic activity, severely limiting PDT's efficiency.[8]

The emergence of nanotechnology in recent years has led to advancements in overcoming the limitation of traditional PDT, which is highly dependent on intertumoral $O_2$ supply. The CDT has emerged as an alternative approach independent of $O_2$ in TME, which produces highly reactive hydroxyl radicals ($^{\bullet}OH$) with significantly stronger oxidation ability than the singlet oxygen.[9,10] Compared to a healthy environment, the TME has a pH that is more acidic due to the generation of large amounts of lactic acid caused by the overactivity of glycolytic metabolism.[11] Further, the TME produces excess $H_2O_2$, where the excessive production of $H_2O_2$ comes from the fast proliferation of the cancer cells and their metabolism.[12–14] Also, $H_2O_2$ is an extracellular and intracellular signalling molecule that influences numerous functions in biological systems as a mediator for several physiological processes, such as cell differentiation and proliferation.[15] The overexpressed $H_2O_2$ and the acidic pH of the cancer environment can be used as the precursor to produce highly reactive $^{\bullet}OH$ for CDT.

In biological treatments, transition metals, such as ferrous ions, are often used to induce CDT *via* Fenton or Fenton-like reactions. Currently, most CDT agents are composed of inorganic nanomaterials, which include potentially toxic metal ions like $Cu^{+}$, $Co^{2+}$, $Ce^{3+}$, and Pd.[16–19] Despite their high catalytic efficiency, these metal ions often pose significant biosafety concerns due to their toxicity.[20] However, the ferrous ion ($Fe^{2+}$) demonstrates moderate catalytic ability in initiating ROS production within the TME, offering a safer alternative. Iron oxide nanoparticles can release ferrous/ferric ions in the form of $Fe^{3+/2+}$, which can catalytically convert $H_2O_2$ into more toxic $^{\bullet}OH$. Fenton reactions necessitate harsh reaction conditions (pH 3–4); furthermore, the mildly acidic TME is insufficient for Fenton reactions to generate ROS.[21] A common strategy to increase the efficiency of the Fenton reaction is by increasing the local concentration of iron oxide or by accelerating the $Fe^{3+}$/$Fe^{2+}$ conversion. An increase in Fenton's reaction rate has been shown to occur in the presence of a light source. UV light has been recognized as a viable method for enhancing the Fenton reaction by regenerating $Fe^{2+}$ from $Fe^{3+}$. However, UV light faces a number of non-legible challenges, such as damage to normal tissues and poor penetration depths due to absorption or scattering, which contribute to low therapeutic efficiency and limit its use in biological systems.[22,23]

Herein, we report a novel Fenton-based cancer therapeutic approach using ND (Fe-doped nanodiamond), which is responsive to NIR light in the biological optical window. The biological component's absorbance coefficient is low in the optical window, so it does not scatter or damage the tissue, resulting in a higher penetration depth. The iron oxide present in ND exists as $Fe^{2+}$/$Fe^{3+}$, which, upon exposure to an NIR laser, can produce more toxic $^{\bullet}OH$ in the presence of $H_2O_2$.[24] First, the interaction and the biocompatibility of FeND with human lung cancer cells (A549) have been studied. In addition, FeND has been assessed against A549 cells for its ability to induce Fenton reaction when exposed to an NIR laser, thereby acting as a therapeutic agent to treat cancer. Apart from being therapeutic, FeND can also be used as a drug carrier to treat cancer. The widely used anthracycline-based drug DOX was loaded onto FeND through physical adsorption. Beyond its therapeutic effects, DOX can elevate the intercellular levels through cascade reactions, which can be utilized for the Fenton reaction to produce more toxic $^{\bullet}OH$.[25]

In our study, FeND is expected to be dual-functional, acting both as a catalyst in the Fenton reaction for cancer therapy and as a carrier for chemotherapeutic drugs. It is anticipated that the catalytic nanoplatform based on the FeND–DOX complex would amplify the cytotoxic mechanism of DOX through a cascade reaction facilitated by the Fenton reaction, promising a new strategy to overcome the limitations of non-specificity and resistance in cancer treatment and furnish an alternative strategy for augmenting the effectiveness of chemotherapy and CDT therapy.

## 2. Experimental section

### 2.1 Materials

Fe-doped nanodiamond (FeND), with an average grain size of 3.5–6.0 nm, was purchased from Ray Technologies, Ltd., Israel. This diamond is synthesized through detonation, then purified and Fe-doped. Fe can be doped onto the ND *via* various techniques such as ion implantation, doping, or surface decoration.[26,27] The specifics of the process used for doping the ND with Fe have not been disclosed by the supplier. Human Serum Albumin (HSA), doxorubicin hydrochloride (DOX), 3-(4,5-dimethylthiazol-2-yl)-2,5-diphenyltetrazolium bromide (MTT), dimethyl sulfoxide (DMSO), 2′,7′-dichlorofluorescin diacetate (DCFH-DA), and hydrogen peroxide ($H_2O_2$) were bought from Sigma-Aldrich (USA). Tetraethylbenzimidazolylcarbocyanine iodide (JC-1) was bought from Abcam, USA, and Fixable Violet Dead Cell Stain Kit was bought from Invitrogen, USA. All chemicals were used as received without further purification.

### 2.2 Characterization of FeND

Evaluation of FeND structural properties was conducted with Raman spectroscopy using a Renishaw 1000B (Renishaw, UK) Raman spectrometer equipped with a 532 nm wavelength CW laser (DPGL-2100F: Photop Suwtech, China). After dispersion in double-distilled (DD) water, the sample was drop-casted onto silicon wafers, dried, and measured under ambient conditions. Further, X-ray photoelectron spectroscopy (XPS) measurements were conducted to observe the elemental composition of the various admixtures present in FeND. The analysis was performed using Thermo K Alpha (Thermo Fisher Scientific, US) fitted with the X-ray source K ALPHA and a multichannel

 

detector. The recorded data was charge shift calibrated using C 1s binding energy and analysed using XPSPEAK41 software.

A superconducting quantum interference device (SQUID, Quantum Design, MPMS-SQUID-VSM, USA) was used to determine the magnetism exhibited by FeND. Specimens were packaged in plastic bags and measured at ambient temperature with a maximum applied magnetic field of 2 T.

### 2.3 FeND–DOX conjugation

DOX was physically adsorbed onto FeND. Pure DOX was dissolved using 4 ml DMSO to a concentration of 12.5 mg $ml^{-1}$ and further diluted in double distilled (DD) water to a final concentration of 30 μg $ml^{-1}$. The diluted DOX was then mixed with FeND in DD water containing 100 μl of 10× pH 7.4 PBS and vortexed for 24 hours, followed by centrifugation at 25 000 rpm for 30 minutes at room temperature to collect the sediments. The collected sediments were redispersed in PBS to wash off the unconjugated DOX and centrifuged. The process was repeated until all the unconjugated DOX were removed from the FeND–DOX complex. The collected supernatant was examined using UV-visible spectrometry (V-750, Jasco, Japan) to quantify the amount of DOX loaded on the surface of the FeND.

$$\text{Drug loading}\% = \frac{\text{initial amount of drug} - \text{unencapsulated drug in supernatant}}{\text{initial amount of drug}} \times 100 \quad (1)$$

**2.3.1 Surface functional group and particle size analysis.** The functional groups present on FeND and FeND–DOX were analysed using a Bomen 100MB FTIR spectrometer (Bomem, Canada) equipped with a liquid nitrogen-cooled MCT detector in ambient conditions. Samples were dispersed in DD water, dropped cast onto silicon wafers, dried, and measured. For particle size analysis, FeND and FeND–DOX were measured using Zetasizer Nano ZS (Malvern Instruments, Malvern, UK) equipped with a 633 nm wavelength He–Ne laser. FeND and FeND–DOX were dispersed in DD water at the concentration of 50 μg $ml^{-1}$ (based on FeND concentration) to measure the particle size.

**2.3.2 The release of drug from FeND.** To study the dissociation and release profile of DOX from the FeND complex in response to the change in pH, the FeND–DOX complex was dispersed into the PBS solution of varying pH of 5, 6, and 7.4 to emulate the cancer microenvironment and the healthy microenvironment. The drug release profile was monitored at 0.5, 1, 3, 6, 12, 24, 48, and 72 h, respectively, using the UV/vis spectrometer, and the percentage of the drug release was calculated from the measured absorption spectra.

### 2.4 Interaction of FeND with cells

Human lung cancer cells (A549) were bought from the Bioresource Collection and Research Centre (BCRC), Taiwan. The obtained cells were cultured in RPMI 1640 medium (GIBCO, USA) with 10% fetal bovine serum (FBS, Gibco, USA). The cell culture was maintained in a humidified incubator at 37 °C and 5% $CO_2$. Cell passages were conducted regularly, and cells were resuspended in fresh media at each passage.

The interaction and the localization of FeND, FeND–DOX, and DOX in A549 cells were visualized using a laser scanning confocal microscope (LSCM SP5, Leica, Germany). The A549 cells were seeded on a cover glass at a density of $5 \times 10^3$. At 70% cell confluence, 20 μg of FeND was added and incubated for 4 h. Subsequently, the cells were washed several times to remove the free FeND particles, which were not taken up by the cells. Finally, the cells were fixed using 1 ml of 4% paraformaldehyde (PFA). The cytoplasm and the nucleus of the A549 cells were dyed with 1 μM per ml DIOC5 and Hoechst, respectively. Finally, the fixed cells were washed with PBS twice, and the colocalization of FeND in A549 cells was visualized *via* LSCM. To find ND areas within cell structures, a z-scan was performed in the vertical direction (Z-scan) in a step of 0.5 μm, with a 40× oil immersion objective.

Two-photon excited fluorescence lifetime imaging (TP-FLIM) was also used to visualize the localization of FeND in A549 cells. A 2D scanner was utilized in conjunction with an Olympus IX 71 inverted microscope (Olympus. Japan) equipped with a UPlanFLN 40× objective lens. The TP-FLIM setup utilized a Ti-Sapphire Chameleon Ultra-II laser (Coherent, Germany) characterized by a pulse duration of 140 fs, repetition rate of 80 MHz, and wavelength range between 760 and 800 nm. Emission spectra within the 450 to 650 nm range were detected using a PicoHarp 300 counting system (PicoQuant, Germany) and a cooled photomultiplier tube (PMT) (PicoQuant, Germany).

A quantitative colorimetric MTT assay was used to evaluate the cytotoxicity of FeND against A549 cells. Cell wells were seeded at a density of $5 \times 10^3$ in a 96 well plate, cultured in normoxic and hypoxic (N: 93%, O: 2%, $CO_2$: 5%) conditions, followed by adding varying concentrations of FeND to the cells. The viability of A549 cells was determined after 24 and 48 h following the addition of particles in the culture medium by adding MTT and incubating for 4 h. Upon incubation, MTT will form purple-coloured formazan crystals. The crystals were dissolved in DMSO, and the absorbance of the solution was measured with an Elisa plate reader, which indicates the number of viable cells.

### 2.5 Extracellular ROS detection

The extracellular ROS generation was confirmed by using methylene blue (MB) dye. Briefly, 100 μg of FeND was added to the solution containing $H_2O_2$ (50 mM) and MB 20 μg $ml^{-1}$ and irradiated with or without an 808 nm laser. Finally, the absorbance change of MB at 664 nm was recorded at an appointed time using a UV/vis spectrometer.

**2.5.1 Photo Fenton-assisted cancer therapy.** To evaluate the therapeutic efficiency of FeND, A549 cells were seeded in a 96 well plate at a density of $5 \times 10^3$ and incubated in normoxic and hypoxic conditions. After 24 h, varying concentrations of FeND were added and incubated for a period of 12 h. The cells were then exposed to an 808 nm wavelength laser with a power density of 0.75 W $cm^{-2}$ for 300 seconds and incubated again for 12 h. After 12 h incubation, an MTT colorimetric assay was used to estimate the efficiency of FeND to annihilate the cancer cells. In addition, we selected a concentration of 100 μg $ml^{-1}$ of FeND and evaluated the effectiveness of laser treatment on A549 cells by varying the durations of laser exposure to three, five, seven, nine, and eleven minutes and subsequently incubated the cells for 12 h. MTT colorimetric assay was used to estimate the effect of the varying laser exposure time on the therapeutic efficiency of FeND.

**2.5.2 Intracellular ROS detection.** The ability to generate $^{\bullet}OH$ by FeND and FeND–DOX complex was evaluated in A549 cells cultured in normoxic and hypoxic environments using fluorescence probe 2,7-dichlorodihydrofluorescein diacetate (DCFH-DA) as an intercellular ROS indicator. The A549 cells were seeded in a 96 well plate at a density of $5 \times 10^3$ followed by adding FeND, FeND–DOX, and DOX complex after 24 h and exposed to an 808 nm wavelength laser for 300 s. After 6 h of the 808 nm wavelength laser exposure, 10 μM of DCFH-DA was added and incubated for 45 min, followed by washing the cells with PBS three times. By evaluating the fluorescence of DCF in an Elisa plate reader, the levels of intercellular ROS were determined.

The intercellular ROS generation was also observed using LSCM. On a glass bottom Petri dish, $5 \times 10^3$ A549 cells were seeded in normoxic and hypoxic environments and incubated for 24 h. FeND, FeND–DOX, and DOX were added and incubated for 12 h and then exposed to an NIR laser for 300 s. Following exposure, the cells were incubated for 6 h, and DCFDA was added. The cells were then incubated for 45 min, and images were taken immediately.

**2.5.3 Mitochondrial membrane potential assay.** FeND's effect on mitochondria in A549 cells was assessed using the JC-1 assay. JC-1 is a green fluorescent monomeric dye to assess mitochondrial damage. In a glass bottom Petri dish, A549 cells were treated with FeND and FeND–DOX for 24 h and exposed to a laser. After 30 min with and without laser exposure, JC-1 dye was added to a glass bottom dish with cells and further incubated in the dark at 37 °C for 30 min. After incubation, the cells were rinsed with PBS, reintroduced with fresh culture medium, and imaged using LSCM. Furthermore, we used the JC-1 to quantify the effect of FeND and FeND–DOX complex on A549 cells seeded in 96 well plates.

**2.5.4 Therapeutic efficiency of FeND–DOX complexes.** To study the therapeutic efficiency of the FeND–DOX complex with and without exposure to 808 nm wavelength laser, A549 cells were used. The cells were seeded at a density of $5 \times 10^3$ in a 96 well plate in normoxic and hypoxic environments, and FeND was added after 24 h of cell incubation. After 12 h of particle incubation, the 808 nm wavelength laser was exposed for a period of 300 s and further incubated for 12 h. A quantitative colorimetric MTT assay was used to determine the efficiency of the DOX-loaded FeND.

**2.5.5 Live–dead assay.** A549 cells were seeded onto the glass bottom dish at a density of $5 \times 10^3$ and incubated for 24 h in normoxic and hypoxic conditions, respectively. The cells were treated with free DOX and FeND–DOX complex and incubated for 24 h before exposing them to NIR laser (808 nm, 0.7 mW $cm^{-2}$) for 300 s. After exposure, the cells were incubated for an additional 12 h, then treated with a Fixable Violet Dead Cell Stain Kit for 30 min, and subsequently imaged using LSCM.

**2.5.6 Statistical analysis.** The statistical significance was ascertained using one-way ANOVA and Dunnett's multiple comparison tests. The error bar denotes the average ± standard deviation. A notable variance between the untreated and treated samples is denoted by $*p < 0.05$, $**p < 0.01$, $***p < 0.001$.

# 3. Result and discussion

## 3.1 Characterization

The crystal structure of the obtained FeND was analysed using Raman spectroscopy. Fig. 1(a) elucidates the $sp^3$ C–C band of a well-defined ND at 1327 $cm^{-1}$, which is noticeably broader and skewed toward lower wavenumbers than its bulk counterpart. The broad asymmetric band centred around 1620 $cm^{-1}$ is attributable to graphitic and amorphous carbon present on the surface, commonly referred to as the G band of ND.[28] The broad peak at around 683 $cm^{-1}$ corresponds to the stretching vibration of Fe–O in the tetrahedral $FeO_4$ configuration of magnetite ($Fe_3O_4$).[29] Within the magnetite spinel structure, the Raman spectra feature five active modes, three of which manifest as weaker peaks. Two such weak peaks are observed at around 302 $cm^{-1}$ and 410 $cm^{-1}$, proximate to the peak associated with the characteristic features of the hematite structure.[29] When magnetite particles are subjected to high laser power or prolonged laser exposure, oxidation can occur. This process induces a phase transition to hematite, attributable to the photolytic effects of the laser.[30] Consequently, it becomes challenging to determine the oxidation state of Fe present on ND by using Raman spectroscopy alone.

XPS was employed to further corroborate these findings by probing the elements and potential admixtures present on the surface of FeND. As evidenced in Table 1, the atomic percentage of Fe on the ND surface is around 3.37%. Transition metals such as Fe are capable of existing in multiple oxidation states. Depending on the ionic state of iron, Fe $2p_{3/2}$ and Fe $2p_{1/2}$ peaks will appear at distinct positions. The binding energies of Fe 2p, as observed in Fig. 1(b), are located at around 709.3 eV and 723.27 eV, which are close to the values found in the literature for the bare $Fe_3O_4$.[31] Moreover, $Fe^{2+}$ and $Fe^{3+}$ ions present in Fe were presumed to produce overlapping Fe 2p spectra, revealing characteristic Fe peaks at specific binding energies.[32] Based on the Raman spectra and XPS measurements as presented in Fig. 1(a) and (b), the iron oxide present on the surface of the ND is most plausibly magnetite, not maghemite.

The magnetic hysteresis behaviour for the as-received FeND was studied using SQUID magnetometry. Fig. 1(c) unveils the

 

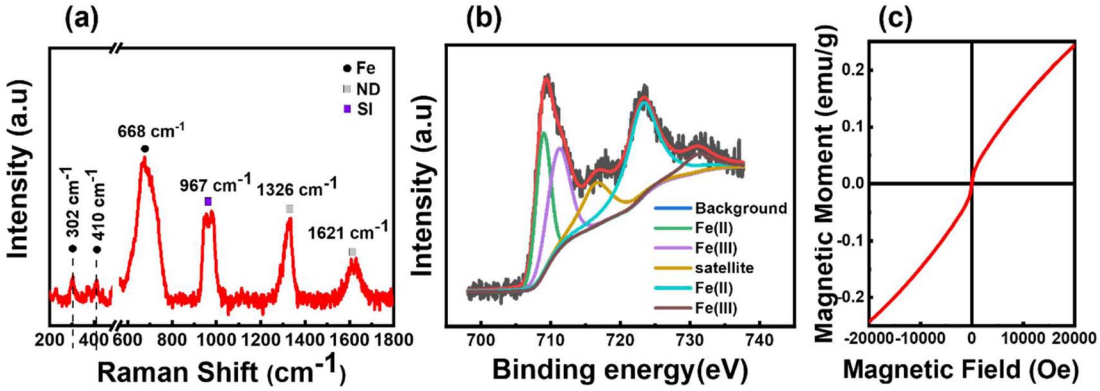


Fig. 1 (a) Raman spectra of FeND powder on Si substrate measured with a Renishaw Raman spectrometer using 532 nm wavelength, revealing the co-existence of Fe and ND phase. (b) Fe 2p spectral analysis of FeND using XPS spectra. (c) Magnetic hysteresis curve of FeND, which shows superparamagnetic nature with unsaturated magnetism up to an applied field of 2 T.

Table 1 The atomic percentage of elements present in FeND analysed using XPS

| | Fe at% | C at% | N at% | O at% |
|---|---|---|---|---|
| FeND | 3.37 | 82.38 | 1.75 | 12.15 |

room temperature superparamagnetic behaviour of FeND, characterized by negligible coercivity and remanence magnetization. Furthermore, FeND exhibits unsaturated magnetic moments up to an applied field of 2 T, a phenomenon potentially attributed to the high carbon content present in NDs, as shown in Table 1. ND exhibits minimal or no net magnetization aligning with the typical behaviour of a paramagnetic material. It is possible that the observed unsaturated magnetic behaviour in FeND arises from interactions between the nonmagnetic ND (diamagnetic) and the superparamagnetic iron oxide, leading to a spin-glass behaviour.[33,34] Superparamagnetism in iron oxide arises when magnetic nanoparticles are in nanoscale dimensions. Each nanoparticle individually displays magnetism within a single domain. In a single magnetic domain, nanoscale dimensions can lead to superparamagnetic behaviour due to the absence of a magnetic hysteresis loop.[35] The presence of iron oxide on ND can enable it as a promising catalyst for the Fenton reaction in tumor settings with high $H_2O_2$ levels. This, combined with FeND's inherent ability to carry drugs can amplify its therapeutic utility.

The widely used anthracyclines class drug DOX for the treatment of cancer was conjugated onto FeND. DOX was noncovalently bound to the surface of FeND *via* physical adsorption (schematically presented in Fig. 1(a)). Fig. 2b represents the light absorbance of the DOX solution before and after conjugation with FeND [residual in the solution], revealing a DOX maximum absorbance at 495 nm. Based on the observed UV-vis absorption spectra and calculation from eqn (1), the estimated amount of drug physically adsorbed onto the FeND surface is approximately 95 ± 2.3% in 100 μg $ml^{-1}$ of FeND. Fourier transform infrared (FT-IR) spectroscopy was utilized to probe the surface functional groups of FeND. Fig. 2c(i–iii) presents a comparative analysis of the FT-IR spectra for FeND, DOX, and the FeND–DOX complex, measured in ambient air. A peak corresponding to the carboxyl group C=O stretching is discernible around 1740 $cm^{-1}$. Additionally, peaks at 1620 $cm^{-1}$ and a broad peak at around 3400 $cm^{-1}$ can be attributed to O–H bending modes of either physically adsorbed water molecules or hydroxy groups on the FeND surface. The C–H stretching observed in the range of 2800 $cm^{-1}$ to 3000 $cm^{-1}$ is ascribable to physisorbed hydrocarbons or loosely bound disordered carbon on the ND surface.[36] FeND exhibits surface groups that are comparable to those of native ND, primarily due to the dominance of carbon as the elemental constituent.[37]

Following the conjugation of DOX with FeND, FT-IR measurement was performed for FeND–DOX to see if there were any changes to the DOX after conjugation. The FT-IR spectra shown in Fig. 2b(iii) reveal the characteristic vibrational modes of DOX molecules in the infrared (IR) spectrum. Upon comparing the FeND–DOX and DOX spectra, absorption features corresponding to the skeletal vibration and the C–H out-of-plane bending vibration of the aromatic rings of DOX are discernible around 1622 $cm^{-1}$ and 800 $cm^{-1}$, respectively. Beyond these two bands, the band identified at 1210 $cm^{-1}$ is indicative of the bending vibrations associated with the CO–H and $CH_x$ groups inherent to DOX. A pronounced signal at 1280 $cm^{-1}$ may be ascribed to the bending vibration of the aromatic ring. Similarly, the peak at 1407 $cm^{-1}$ is attributable to the vibrations of the aromatic ring. The breathing vibrations of aromatic entities were notably observed at 1578 $cm^{-1}$. The band at 1615 $cm^{-1}$ corresponds to the stretching vibration of the aromatic ring coupled with the CO–H group. The band situated at 1724 $cm^{-1}$ can be associated with the N–H bending vibration emanating from the amino moiety, suggesting that the structural conformation of DOX remains unaltered after conjugation with FeND. Through electrostatic interactions and hydrogen bonding, carboxylic groups on the ND surface can undergo deprotonation and protonation with amine functional groups in the DOX molecule, resulting in stable ND–DOX complexes.[38] Following conjugation, the size of the FeND particles increased from 129.3 ± 19.81 nm to 140.2 ± 23.09 nm, as illustrated in Fig. 2d and e.

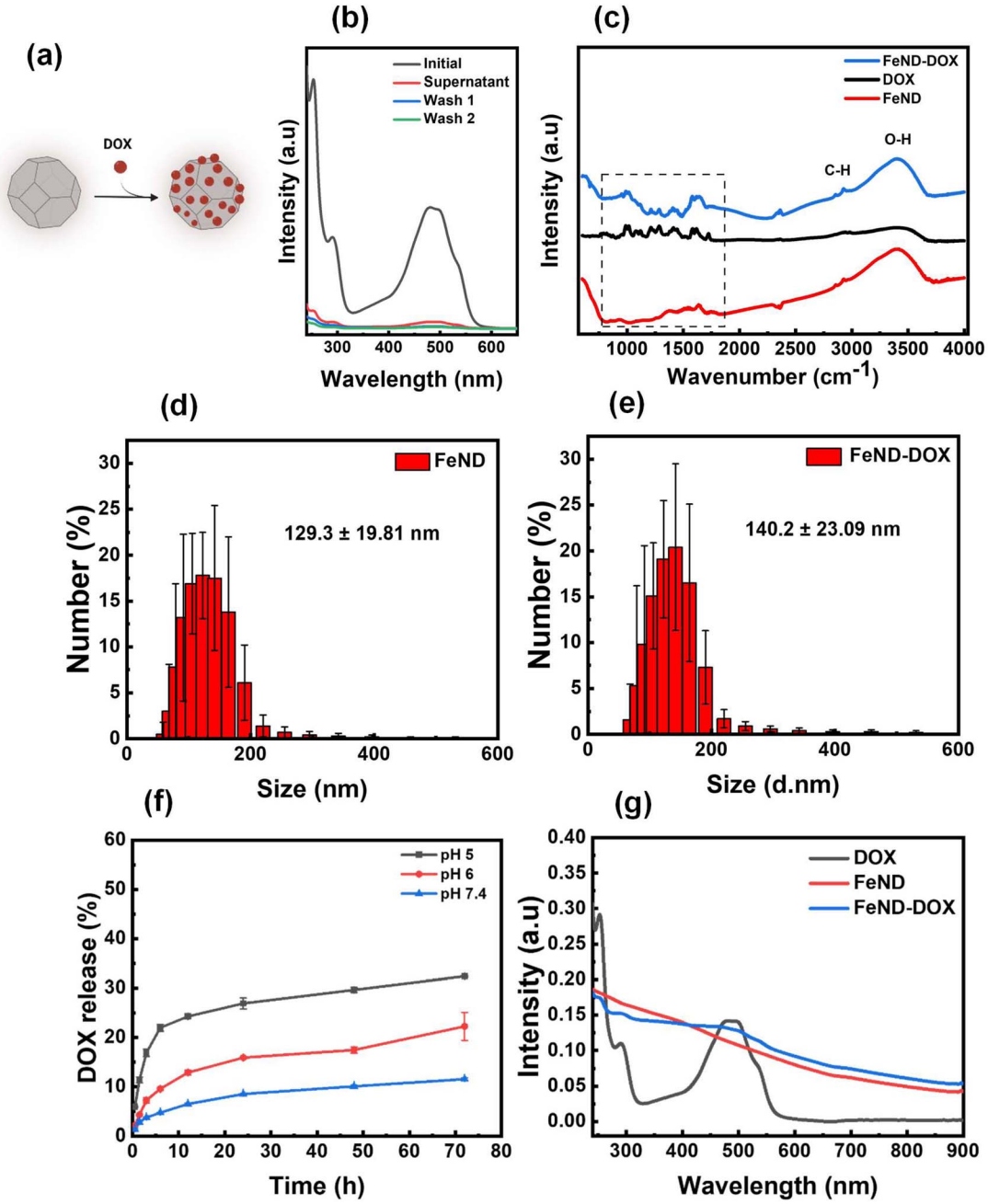


Fig. 2 (a) Schematic illustration of FeND conjugation with DOX. (b) UV/vis spectra of the conjugation of FeND with DOX. (c) FTIR spectra of FeND, DOX, FeND-DOx complex. Particle size distribution (d) and (e). (f) The percentage of the drug released at pH 7.4, pH 6, and pH 5 at intervals of 0.5, 1.5, 3, 6, 12, 24, and 48 h, respectively. (g) The absorbance spectra of DOX, FeND, and DOX–FeND, $N = 3$.

Following the conjugation of DOX with FeND, it is essential for the DOX to be released from the FeND surface for its effective anticancer therapeutics. The drug-release behaviour of DOX from FeND was evaluated in phosphate-buffered saline (PBS) at varying pH levels of 7.4, 6, and 5 to mimic conditions in both normal physiological and cancerous microenvironments. Fig. 2f illustrates the release of DOX from the FeND surface. Across all examined pH levels, FeND facilitated a slow and consistent release of DOX. As the pH decreases, the dissociation of the drug from FeND increases rapidly, indicating that the acidic environment is effective for releasing far more drug. In such acidic conditions, an abundance of hydrogen ions ($H^+$) can interact with the carboxylate ($COO^-$) groups of the complex, consequently displacing the protonated DOX (doxorubicin–$H^+$) from the carboxylate groups. This mechanism can be interpreted as competitive binding of free $H^+$ ions to the FeND's surface $COO^-$ group under acidic conditions. As a consequence of these interactions, DOX is released from the complex more rapidly in acidic environments compared to basic environments.[39] Additionally, Fig. 2g illustrates the UV-vis spectra following the successful encapsulation of DOX onto FeND, with

both FeND and FeND–DOX manifesting a significant near-infrared (NIR) absorption.

### 3.2 Interaction of FeND with cells

To confirm the uptake of FeND by the A549 cells, the intracellular localization of FeND in A549 cells was investigated through LSCM. Fig. 3(a) presents LSCM images of FeND interactions with A549 cells following a 12 h incubation period. The localization of ND in individual cells can be determined by a series of confocal fluorescence image scans taken along the *z*-direction (*z*-scan). In these images, the nuclei of the dyed A549 cells are depicted in blue, while the cytoplasm is in red. The

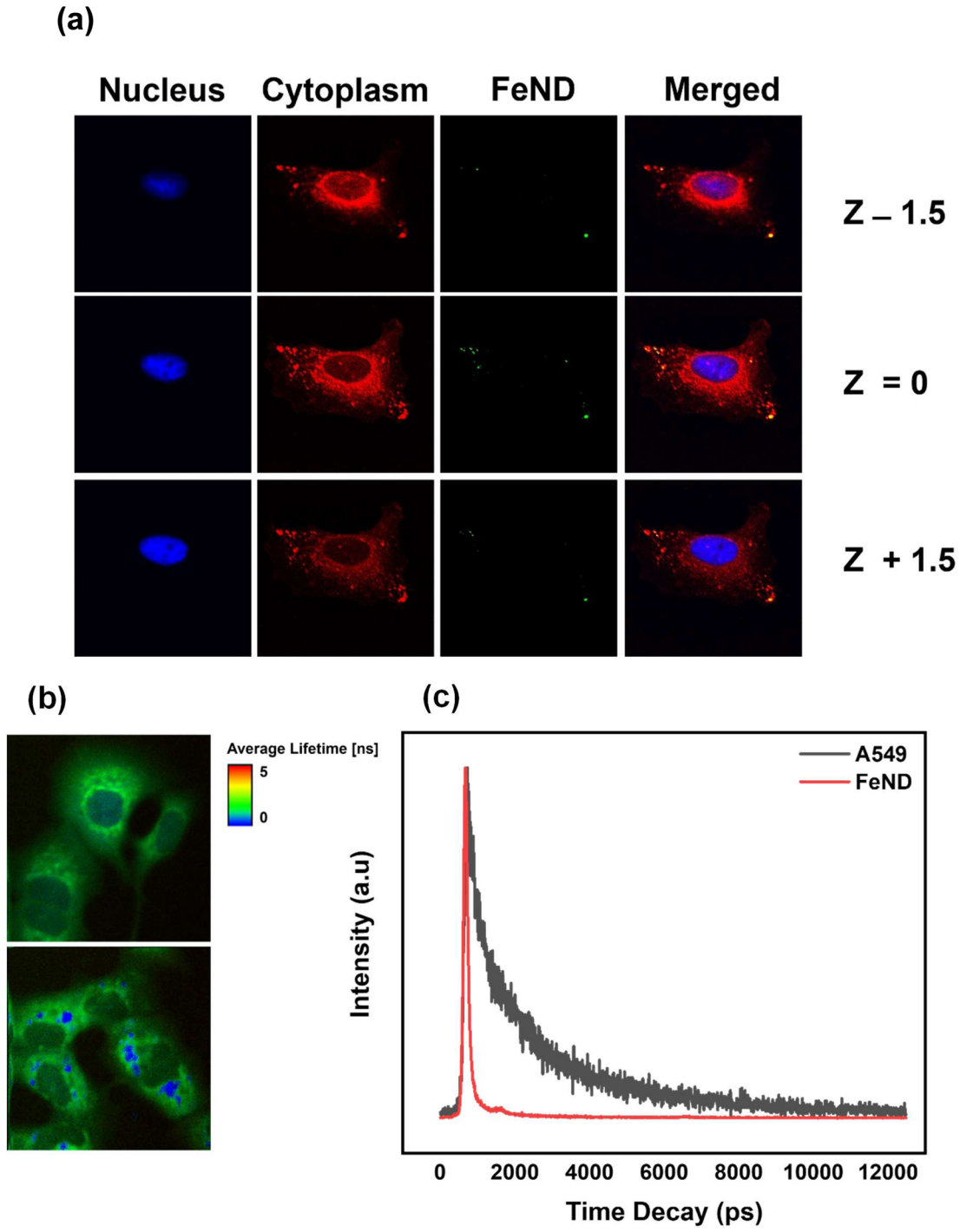


Fig. 3 (a) FeND interaction with A549 cells imaged using laser confocal fluorescence images captured through a stepwise Z-scan at intervals of 1.5 μm. For LSCM, cell cytoplasm was stained with Hoechst and the cell cytoplasm was stained with DIOC5, respectively. Two-photon fluorescence lifetime image of (b) A549 cells and (c) A549 cells incubated with FeND. (c) Fluorescence lifetime decays for FeND fluorescence and A549 cell autofluorescence using two-photon excitation.

fluorescence emitted from FeND is visualized in green. The fluorescence in ND is primarily due to defects in the core and on the surface, which are highly photostable and resistant to photobleaching.[37] Based on the z-scan images presented in Fig. 3(a), it is demonstrated that FeND efficiently penetrates the A549 cells and localizes within the cytoplasm. This is corroborated by the yellow colour observed in Fig. 3(a), which is an overlay of the green from FeND and red fluorescence from the cell cytoplasm correspondingly. The internalization of the ND's within A549 cells is facilitated through energy-dependent, clathrin-mediated endocytosis.[40]

Additionally, we employed two-photon fluorescence lifetime imaging microscopy (TP-FLIM) to visualize the intracellular penetration of Fe–ND. For FLIM analysis, the cells were not dyed. FLIM images, presented in Fig. 3(b), depict both untreated A549 cells and those exposed to FeND. As illustrated in Fig. 3(b), FeND is well observed in FLIM, which enables the FeND location inside the cell to be defined. This observation is consistent with the findings obtained through LSCM, as depicted in Fig. 3(a), where Fe–ND is also localized within the cytoplasm. Furthermore, Fig. 3(c) compares the fluorescence lifetime of Fe–ND with the autofluorescence lifetime of the cells. Fe–ND exhibits a markedly shorter fluorescence lifetime of 0.7 ns, contrasting the 1 to 3 ns lifetime typically observed in cellular autofluorescence. This marked difference distinguishes FeND from autofluorescence. This characteristic allows FeND to be easily distinguished and utilized as a fluorescent marker.[41,42]

A particle intended for biological applications must demonstrate strong biocompatibility and minimal cytotoxicity. The biocompatibility of FeND and DOX was evaluated on A549 cells under both normoxic and hypoxic conditions using the MTT assay. Fig. 4 elucidates that FeND particles, when incubated with

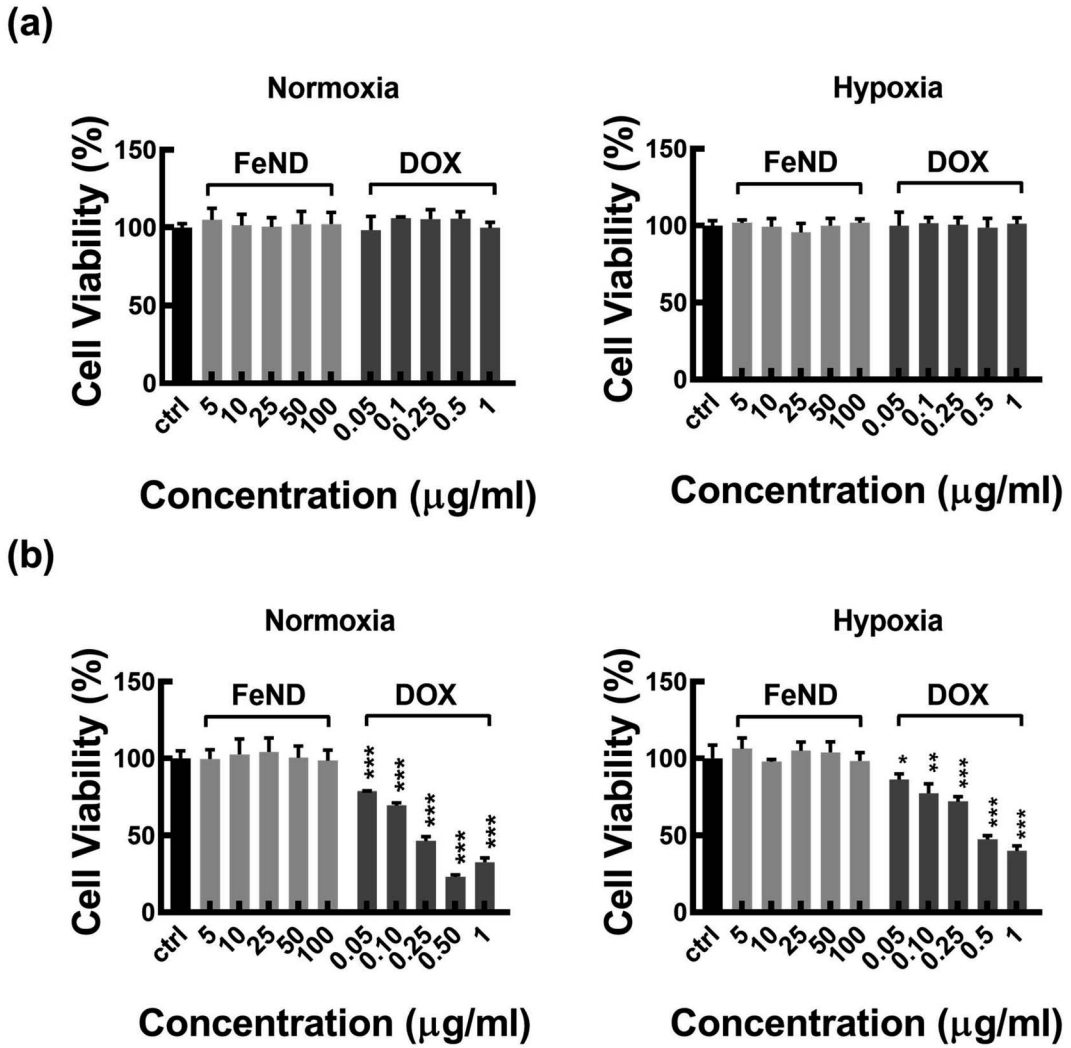


Fig. 4 The cytotoxicity of FeND and DOX at different concentrations was evaluated against A549 cells in normoxic and hypoxic condition and then examined using MTT assay for (a) 24 and (b) 48 hours. $N = 3$. FeND showed no toxicity towards A549 cells in both normoxic and hypoxic conditions, while DOX demonstrated minimal toxicity at 24 hours. However, its toxicity increased with higher doses and longer exposure, inversely affecting cellular viability. Statistical relevance was assessed using one-way analysis of variance along with Dunnett's multiple comparison tests. The bar represents mean ± SD. Significant difference between untreated and treated samples is indicated by *$p < 0.05$, **$p < 0.01$, ***$p < 0.001$.

A549 cells, demonstrate negligible toxicity across the concentration range employed in contrast to many other metal or metal oxide nanoparticles, which exhibit dose-dependent cytotoxicity.[43] On the other hand, the anticancer agent DOX exhibited a negligible level of toxicity at 24 h. However, its toxicity became more pronounced with increasing concentration and longer exposure time, with cellular viability being inversely proportional to DOX concentration. In a hypoxic environment, A549 cells exhibited resistance to DOX at 48 h of exposure, in contrast to their behaviour in a normoxic environment. This resistance is ascribed to a multifaceted set of factors, such as the limited availability of $O_2$, which is essential for the effectiveness of the anti-tumor drugs, exacerbated DNA over-replication, increased genetic instability, and the inhibitory effects of hypoxia on cell proliferation.[44] Additionally, elevated expression of the multi-drug resistance (MDR) transporter P-glycoprotein contributes to this resistance.[45] Predominantly, resistance is further intensified by the upregulation of gene transcription mediated by hypoxia-inducible factor 1 (HIF-1).[46] Consequently, subsequent studies were conducted using a 20 μg concentration of DOX, which gives less than 50% cell viability in normoxic conditions after 48 h of incubation with A549 cells.

### 3.3 ROS generation by FeND

The catalytic efficiency of FeND in converting $H_2O_2$ to ˙OH was evaluated using MB dye. Fig. 5(a) illustrates the schematic representation of both the classical and photo-Fenton reactions. In the classical Fenton reaction, iron oxide nanoparticles can react with $H_2O_2$, resulting in the production of ˙OH through redox reactions involving $Fe^{2+}$ and $Fe^{3+}$ under low pH conditions.[21] In a cellular environment, pH is around 5–7.4, at which it is not possible for the classical Fenton to proceed. The photo-Fenton reaction enhances this process by harnessing light energy to stimulate the generation of ˙OH. The light facilitates the continuous regeneration of iron catalysts and promotes the formation of additional radicals from hydrogen peroxide. This results in a more efficient production of reactive species, which can amplify the therapeutic effects and potentially enhance the efficiency in eliminating the cancer cells.[23] The potential of FeND to generate ROS was assessed using MB dye as an indicator. A typical product of a Fenton reaction was the production of highly reactive ˙OH. The production of ˙OH by FeND through the Fenton reaction, with and without laser exposure, was determined by monitoring the absorption of MB at 664 nm, as the produced ˙OH can oxidize and degrade the MB. As depicted in Fig. 5(b) and (c), MB absorption remained unchanged when mixed with $H_2O_2$ for a period of 20 min. However, upon the addition of FeND, the absorption intensity of MB decreased by around 11.2% in the presence of $H_2O_2$, indicating that FeND and $H_2O_2$ interact to form ˙OH. Exposure of FeND to a laser further accelerated the degradation rate of MB, likely attributable to the photoreduction of $Fe^{3+}$ to $Fe^{2+}$, thereby enhancing

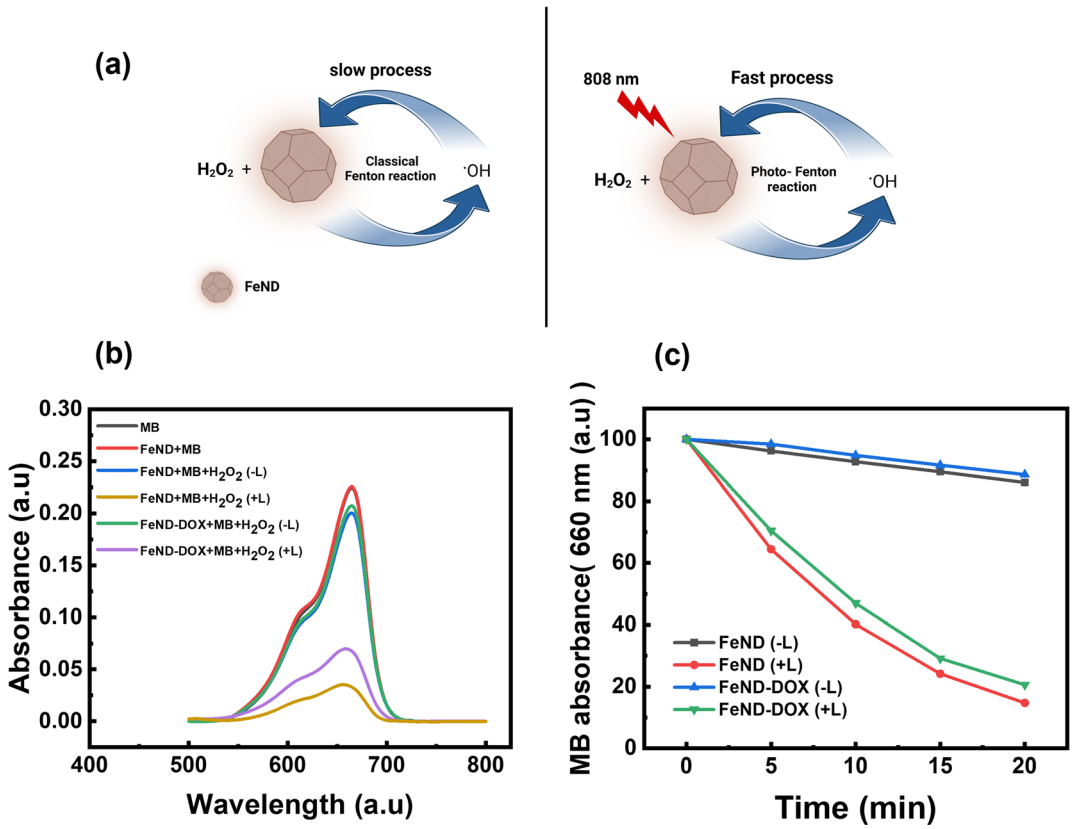


Fig. 5 (a) Schematic representation of the photo Fenton reaction. (b) UV-vis spectra of MB solutions treated with or without $H_2O_2$ and FeND and FeND–DOX with or without the 808 nm laser for 20 min. (c) Degradation rate of MB treated with $H_2O_2$, FeND, and FeND–DOX at intervals of 5 min for 20 min with or without laser. FeND and FeND–DOX exposed to laser showed significant MB degradation when exposed to laser.

Fenton efficiency. Additionally, when DOX-conjugated FeND was laser-exposed, the degradation of MB remained similar, suggesting that the surface conjugation of DOX to FeND did not impede the Fenton reaction.

### 3.4 Intracellular ROS generation

To explore FeND's potential in ROS generation within A549 cells, 808 nm wavelength laser irradiation was employed, utilizing the well-established indicator DCFH-DA.[47] In the intracellular environment, ˙OH formed during the Fenton reaction can oxidize non-fluorescent DCFH-DA molecules into fluorescent DCF molecules. Fig. 6(a) presents the results of intracellular ROS generation in A549 cells under both normoxic and hypoxic conditions following incubation with FeND with and without exposure to near-infrared (NIR) laser. Fig. 6(a) reveals that FeND-incubated A549 cells, when exposed to NIR laser, exhibited a markedly elevated level of ROS compared to non-exposed cells. This elevation in ROS can be attributed to the laser-enhanced conversion of $Fe^{3+}$ to $Fe^{2+}$ within FeND, transforming intercellular $H_2O_2$ into more reactive ˙OH, thereby amplifying fluorescence intensity relative to FeND-treated but non-laser-exposed cells. $H_2O_2$ is generated within cells as a by-product of cellular metabolism due to the incomplete reduction of $O_2$ in the electron transport chain of mitochondria during cellular respiration.[48]

Based on the results of the experimental evaluation of FeND's ability to facilitate ROS generation in A549 cells, we further explored its efficacy in inducing cell death in these cells *via* photo-Fenton reactions. The A549 cells were co-incubated with varying concentrations of FeND and subsequently exposed to an NIR laser for 300 s. Fig. 6(b) shows the cell viability as assessed by the MTT assay. As anticipated, A549 cell viability declined in correlation with increased FeND concentration when subjected to NIR laser exposure. This decline can be attributed to the catalytic conversion of intracellular $H_2O_2$ into more toxic ˙OH by iron oxide in FeND by undergoing redox

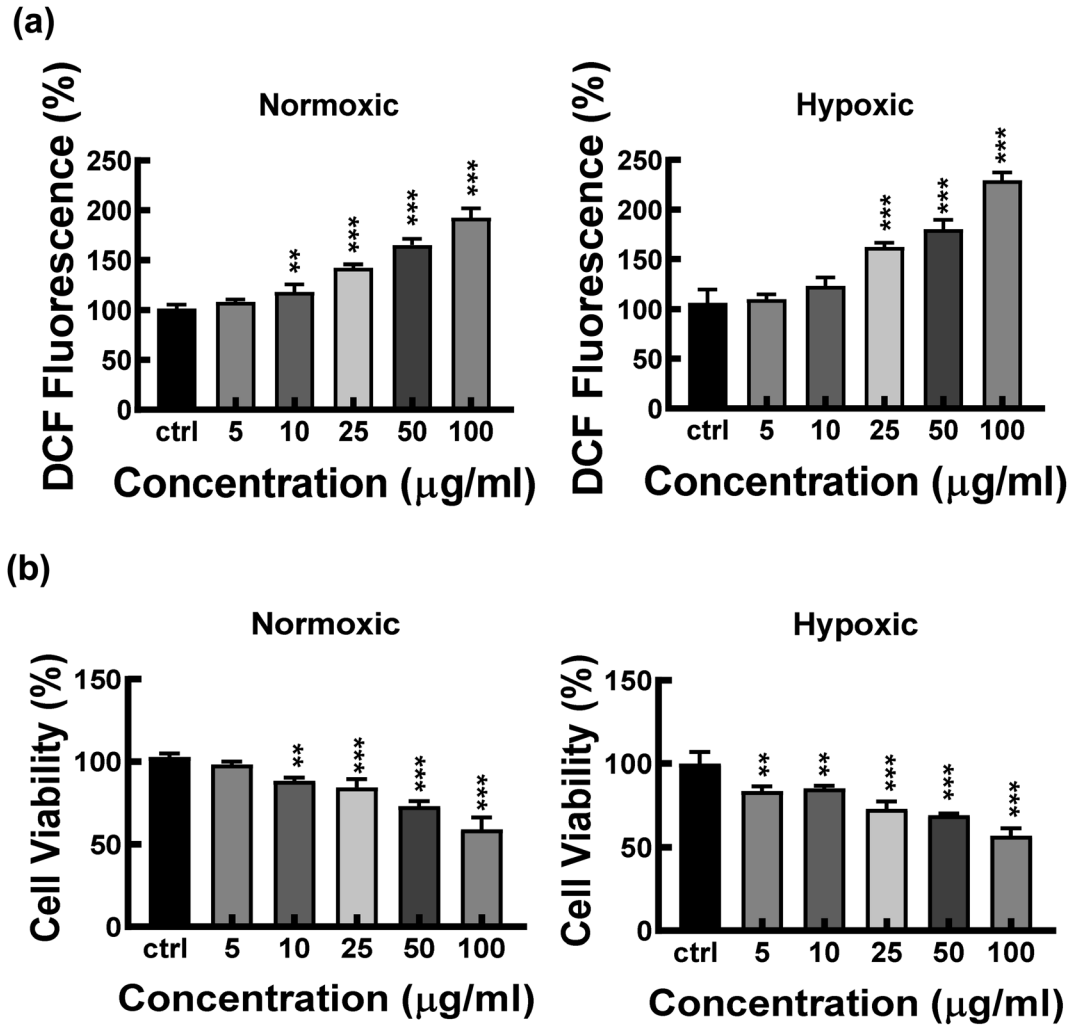


Fig. 6 (a) Intracellular ROS generation of FeND incubated with A549 cells and exposed to 808 nm laser in normoxic and hypoxic tumour environments. (b) Cell viability of A549 cells treated with different concentrations of FeND and exposed to 808 nm laser in normoxic and hypoxic cellular environment. Statistical relevance was assessed as mentioned in Section 2.5.6. The bar represents mean ± SD. Significant difference between untreated and treated samples is indicated by $*p < 0.05$, $*p < 0.01$, $***p < 0.001$.

 

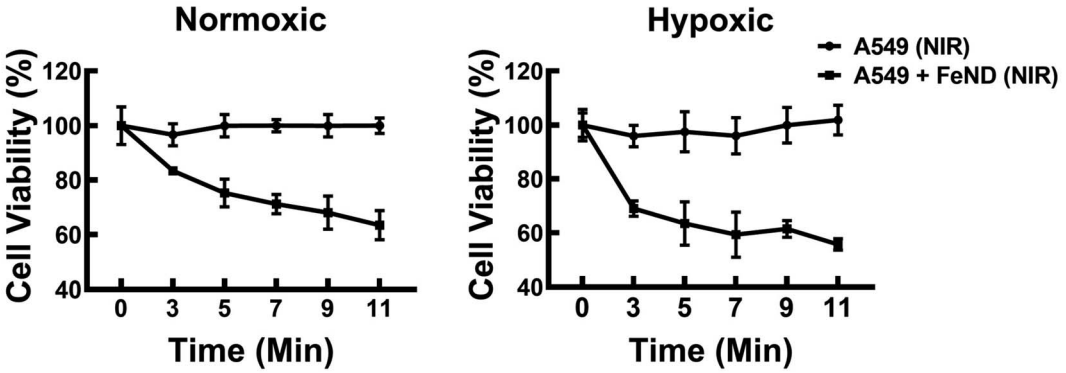


Fig. 7 Cell viability of A549 cells and A549 cells incubated with FeND exposed to varying 808 nm laser exposure time. Increasing the laser exposure time on A549 cells incubated with FeND did not show any significant difference. Statistical relevance was assessed as mentioned in Section 2.5.6. The bar represents mean ± SD. Significant difference between untreated and treated samples is indicated by $*p < 0.05$, $*p < 0.01$, $***p < 0.001$.

reaction. These $^{\cdot}OH$, upon formation, can interact with intracellular components, thereby inducing cell death or apoptosis.[9]

Notably, this effect was not observed when the cells were incubated with the particle but not exposed to the NIR laser. This lack of effect is likely due to the cessation of the Fenton reaction once all $Fe^{2+}$ ions are consumed.[24] This potential cessation of the Fenton reaction could be due to the slow conversion rate of $(0.002–0.01\ M^{-1}\ s^{-1})$ from $Fe^{3+}$ back to $Fe^{2+}$.[49] In FeND, Fe in ND can undergo a redox reaction to produce $^{\cdot}OH$ and forms $Fe^{2+}$ and $Fe^{3+}$. The reduction of $Fe^{3+}$ to $Fe^{2+}$ is a rate-

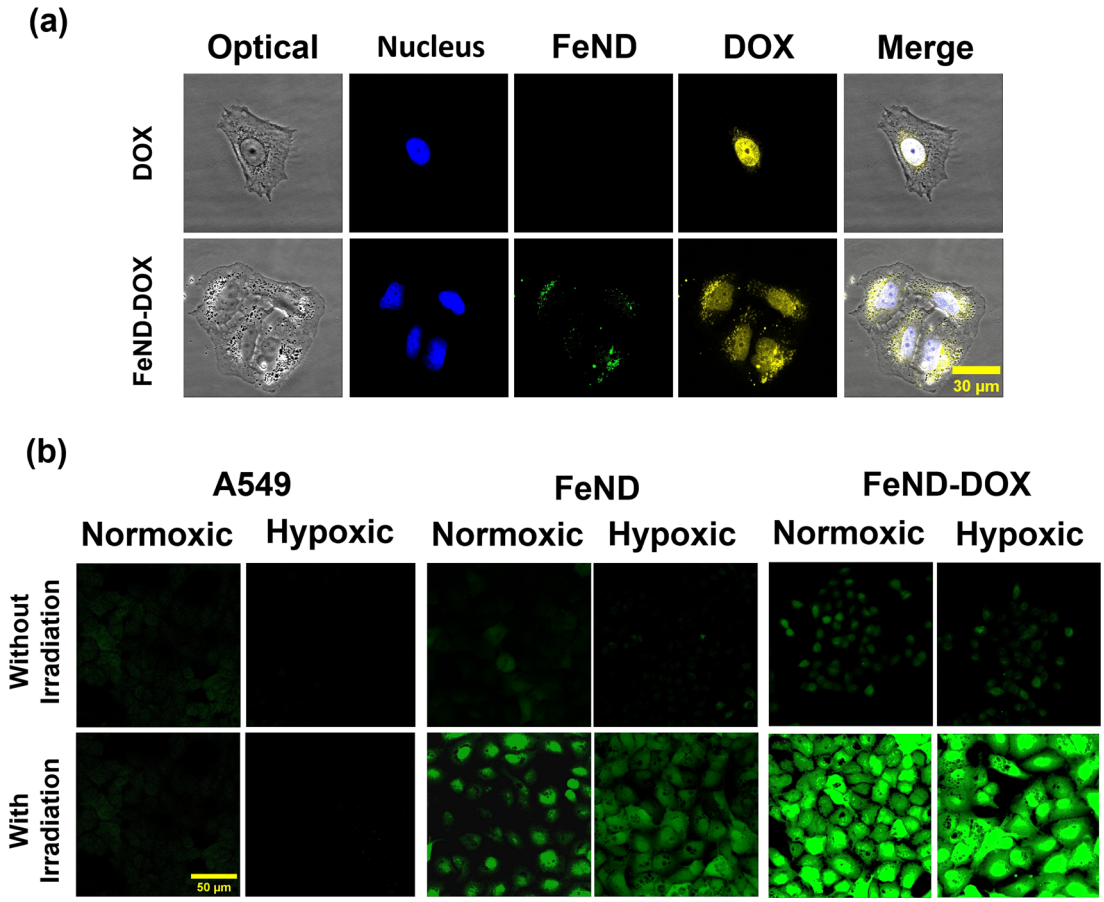


Fig. 8 (a) Laser confocal fluorescence images illustrating the interaction between DOX, FeND–DOX, and A549 cells. (b) Confocal images for visualizing ROS in normoxic and hypoxic A549 cells treated with FeND and FeND–DOX, with and without laser exposure, determined using DCFH-DA assay. FeND–DOX incubated A549 cells showed enhanced ROS production.

limiting step that occurs when the pH is less than 4,[21] which is not possible in a cancerous environment in which the pH is between 5 and 7.[50,51] When FeND is exposed to the NIR laser, the regeneration of $Fe^{2+}$ by photoreduction of $Fe^{3+}$ can occur.[51] This process leads to increased production of $^{\bullet}OH$, leading to a decrease in cell viability. In addition, the catalytic efficiency of FeND is also affected by the concentration of iron ions, which can greatly reduce its therapeutic effectiveness.[51,52] As can be seen from Fig. 6(b), the cell viability is only reduced to a certain extent.

Subsequently, the effects of laser exposure on Fe–ND-incubated A549 cells were evaluated using varied laser exposure times. Fig. 7 illustrates the cell viability of A549 cells with varying laser exposure times (3, 5, 7, 9, and 11 min), as estimated from the quantitative colorimetric MTT assay. Based on the observed cell viability, it can be concluded that increasing exposure times did not result in a significant decrease in cell viability. However, this lack of significant change may possibly be ascribed to the limited levels of endogenous $H_2O_2$ generated within the cellular environment.[53] To address the limitations of endogenous $H_2O_2$ levels, we have conjugated FeND with DOX. The DOX can work in various ways to inhibit the growth and division of cancer cells, such as DNA intercalation, inhibition of topoisomerase II, free radical production *etc.*[54] The DOX was employed to augment intracellular $H_2O_2$ levels while concurrently serving as an anticancer agent.[25] The drug concentration for the photo-Fenton reaction was determined based on the value derived from Fig. 5.

The ability of FeND to deliver and release DOX within the A549 cells was assessed before examining the mediation of intracellular ROS generation by the FeND–DOX Fenton reaction. The CLSM images in Fig. 8(a), which display DOX fluorescence in red, reveal that upon internalization, FeND–DOX particles successfully released DOX into the cytoplasm and penetrated into its designated site of action within the A549 cells. These findings substantiate that FeND can be efficiently internalized by A549 cells and facilitate drug release into the cytoplasm. Further visualization of intracellular ROS was accomplished using LSCM. Fig. 8(b) shows the comparative analysis of ROS generation in cells treated with FeND, DOX, and FeND–DOX, both with and without exposure to NIR laser. As anticipated, in LSCM images, cells incubated with FeND demonstrated elevated ROS production upon NIR laser illumination. When FeND was conjugated with DOX and subjected to NIR laser, a significant increase in ROS production within A549 cells was observed *via* LSCM images. After the dissociation of DOX from FeND inside the cells, the anthracycline-based DOX can undergo a series of redox reactions, resulting in the formation of DOX–semiquinones and superoxides. This process elevates intercellular $H_2O_2$ levels, which are subsequently

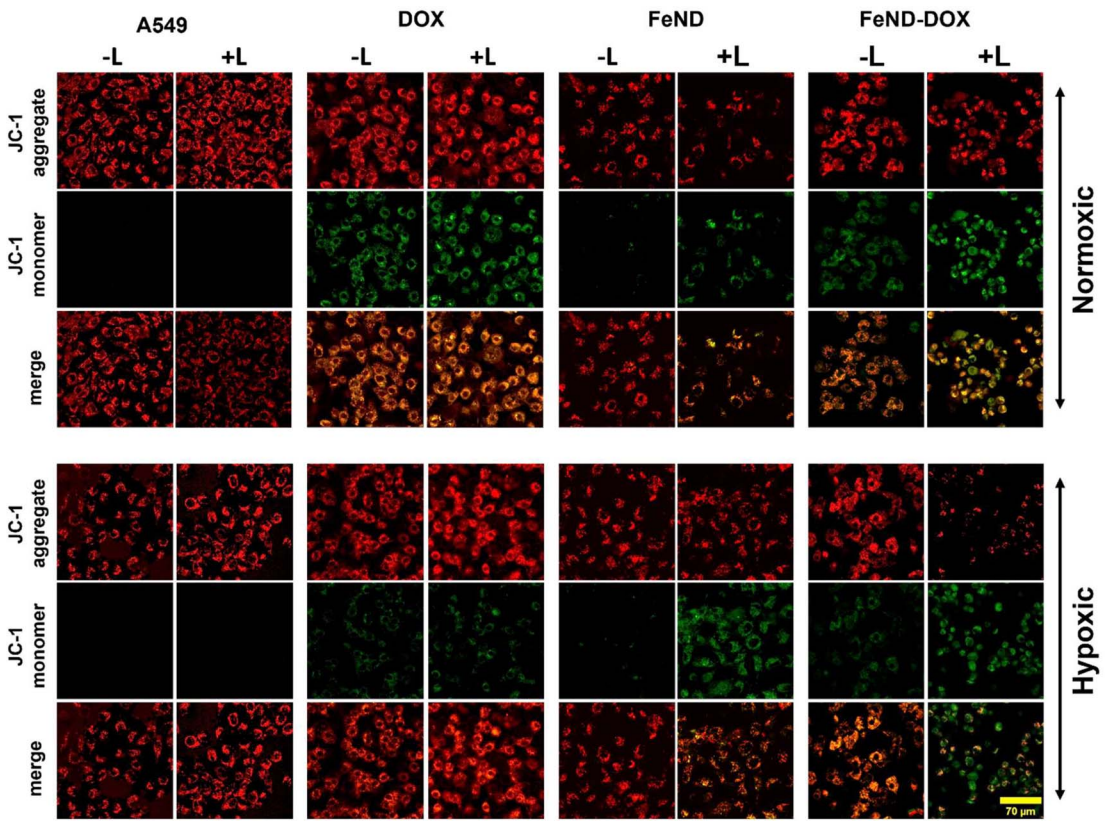


Fig. 9 Assessment of mitochondrial depolarization using JC-1 die using LSCM in normoxic and hypoxic conditions for 36 h, with (+) and (−) without laser exposure. The red colour of the JC-1 aggregate signifies healthy cells with high MMP, while the green colour of the JC-1 monomer indicates cells with low MMP.

converted into ˙OH *via* the photo-Fenton reaction mediated by iron ions in FeND. Thus, DOX serves a dual role as an anticancer agent and as a catalyst for enhanced $H_2O_2$ production, which is further utilized in the Fenton reaction upon laser exposure of the FeND–DOX complex. However, as is seen in Fig. 4(b), the hypoxic condition of TME limits the potential of DOX to induce an anticancer effect and to produce $H_2O_2$ in A549 cells due to low $O_2$. In such hypoxic TME, $H_2O_2$ is abundant, ranging from 0.1 mM to 1 mM, and the accumulated $H_2O_2$ inside the cells can be utilized by the internalized FeND to produce endogenous $O_2$, thereby facilitating the activation of DOX.[48,55,56] This activation further augments intracellular $H_2O_2$ levels, promoting the production of additional ˙OH.

The mechanism of ROS-mediated cell death is investigated as mitochondria play an essential role in apoptosis, particularly in response to stress. Fig. 9 shows a visual analysis of mitochondrial damage induced by FeND, DOX, and FeND–DOX, both with and without laser exposure, as assessed by the JC-1 assay using LSCM. In healthy mitochondria with intact membrane potential, the cationic JC-1 dye aggregates inside the mitochondria, exhibiting a characteristic emission at red wavelengths (~590 nm). Conversely, a compromised mitochondrial membrane potential results in the dispersal of JC-1, manifesting as green fluorescence (~525 nm). A change in mitochondrial membrane potential serves as an early indicator for apoptosis.[57] Fig. 9 shows that both control cells and the cells incubated with FeND without laser exposure display a robust JC-1 aggregate signal, indicating healthy mitochondria. In contrast to control cells, which exhibited stable mitochondrial membrane potential as evidenced by strong JC-1 aggregate

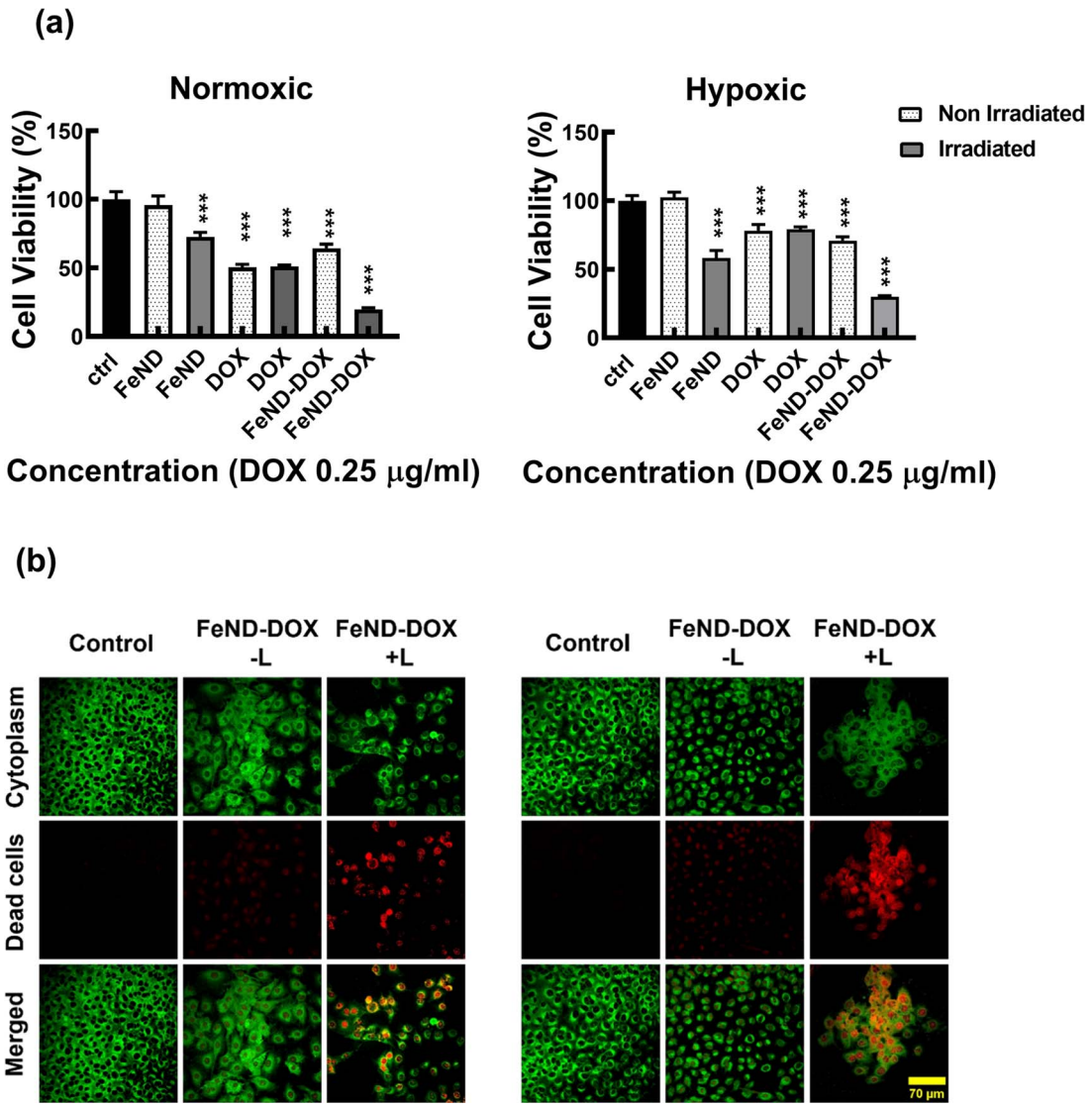


Fig. 10 Cytotoxicity of FeND–DOX with and without exposure to 808 nm laser. (a) Cytotoxicity of FeND–DOX with and without exposure to 808 nm laser. (b) Fluorescence images of a live/dead assay of A549 cells 12 h after with and without exposure to laser. The FeND–DOX complex showed pronounced toxicity when exposed to NIR laser in both normoxic and hypoxic conditions compared to free DOX and FeND–DOX (without laser exposure). Statistical relevance was assessed as mentioned in Section 2.5.6. The bar represents mean ± SD. Significant difference between untreated and treated samples is indicated by *$p$ < 0.05, *$p$ < 0.01, ***$p$ < 0.001.

fluorescence, cells treated with FeND and subjected to NIR laser exposure displayed a marked reduction in mitochondrial membrane potential. This phenomenon is likely due to the increase in oxidative stress induced by the Fenton reaction, potentially resulting in damage to the mitochondria. Similarly, treatment with DOX also led to a reduction in mitochondrial membrane potential, corroborated by changes in JC-1 fluorescence, as seen in Fig. 9, which is likely attributable to ROS production.[58,59] Unlike the control cells, which maintained membrane integrity as seen by consistent JC-1 aggregate formation, DOX-treated cells showed compromised mitochondrial membrane potential, substantiated by a discernible shift from red to green fluorescence. Notably, A549 cells treated with FeND–DOX and exposed to laser exhibited pronounced mitochondrial depolarization compared to those treated with FeND or DOX alone upon laser exposure. This can be attributed to the excess generation of ROS by photo-Fenton reaction, arising from the enhanced production of $H_2O_2$ within the cells due to DOX, as illustrated in Fig. 8(a).

### 3.5 Fenton-induced cancer therapy

Based on the aforementioned results, we hypothesized that the Fe–ND-facilitated enhanced CDT pathway, coupled with the chemotherapeutic effects of DOX, could more proficiently induce cancer cell apoptosis in both hypoxic and normoxic conditions. To assess the efficacy, the FeND–DOX complex was compared with free DOX in terms of its ability to induce toxicity both in the presence and absence of laser exposure. Fig. 10(a) displays the cell viability of A549 cells incubated with free DOX, FeND, and the FeND–DOX complex, with and without laser exposure, in both normoxic and hypoxic conditions, as determined by the MTT assay. In a hypoxic environment, DOX exhibited reduced toxicity toward A549 cells when compared to its effects in a normoxic environment. Conversely, FeND–DOX showed similar toxicity levels but were slightly less toxic than free DOX at the same dosage. This difference is attributable to the fact that free DOX can rapidly diffuse through cells and intercalate with DNA to inhibit DNA replication and cell growth, while the FeND–DOX complex must penetrate the cells and gradually release the drug to exert its desired effect, as illustrated in Fig. 2(f) and 8(a).[42,60]

We compared the role of CDT mechanism by FeND along with the combined role of CDT and chemotherapeutic drug in FeND–DOX with and without laser exposure. FeND-treated cells exposed to NIR laser showed around a 30% decrease in cell viability, while the non-exposed FeND-treated A549 cells showed no toxicity. However, FeND loaded with DOX without NIR laser exposure produced comparable toxicity as that of the free DOX. When exposed to a NIR laser, as shown in Fig. 10(a) and (b), FeND–DOX induced a significant amount of toxicity, reducing the cell viability by around 80% in both normoxic and hypoxic conditions. These findings suggest that DOX plays a crucial role in the CDT pathway under normoxic conditions. When the hypoxic environment hampers the chemotherapeutic pathway of DOX, CDT serves to amplify its synergistic interaction with DOX's chemotherapy. The combination targets various cellular mechanisms and is expected to enhance the overall efficacy of treating cancer cells. This desired outcome could be attributed to the interplay between the Fenton reaction and the chemotherapeutic and $H_2O_2$ generation efficiency of DOX. Overall, the FeND–DOX complex demonstrated excellent antitumor activity in both hypoxic and normoxic environments through synergistic CDT and chemotherapy. Additionally, this combined approach may allow for a reduction in the dosage of DOX without sacrificing therapeutic efficacy.

## 4. Conclusions

In summary, this study focuses on the role of FeND in cancer therapy. Raman spectroscopy and XPS analyses confirmed the presence of magnetite $Fe_3O_4$ on the surface of ND. A key component of Fe–ND is carbon, which possesses diverse functional groups. Through these groups, the chemotherapeutic drug DOX was physically adsorbed onto the surface without compromising its functional properties. By utilizing the inherent fluorescent properties of ND, we were able to visualize the biodistribution of FeND in A549 cells. Notably, these particles effectively released DOX into the A549 cell cytoplasm. FeND enabled the Fenton reaction, leading to the generation of ROS. The process was augmented by near-infrared (NIR) laser exposure, indicating the applicability of FeND in enhanced CDT. FeND demonstrated an ability to generate ROS, particularly when exposed to NIR laser. The catalytic Fenton efficacy of FeND was not compromised upon conjugation with DOX. Significantly, the conjugation of DOX not only served as an anticancer agent but also synergistically elevated intracellular $H_2O_2$ levels, thereby augmenting the Fenton reaction.

This therapeutic combination was efficient in both hypoxic and normoxic conditions. Importantly, the CDT pathway amplifies the efficacy of DOX, especially when its chemotherapeutic effectiveness is suppressed in hypoxic environments. This augmentation is postulated to be mediated by the Fenton reaction, enhancing DOX's chemotherapeutic effects. This combined FeND–DOX complex showcased amplified therapeutic potential. The combined CDT and chemotherapeutic approach yielded a synergistic effect, enhancing antitumor activity. Such findings underscore the potential of FeND–DOX as a promising candidate for improved cancer therapy. This integrated approach not only elevates therapeutic efficacy but also expands its applicability to both normoxic and hypoxic tumor conditions. Consequently, FeND–DOX emerges as a promising candidate for imaging-guided cancer therapy.

This multifaceted capability provides a means to target and treat cancer cells more effectively while potentially reducing the side effects associated with conventional chemotherapy. Its effectiveness and targeted drug delivery method establish it as a valuable candidate for personalized cancer therapy, meriting further exploration in preclinical and clinical studies. Considering these results, the FeND–DOX composite shows significant promise as a CDT agent. We propose further research, particularly focusing on delivering CDT into a mice model, to understand how FeND enhances CDT efficiency in hypoxic tumor environments. This research is vital for advancing

biomedical applications and offers insights into potential improvements in cancer treatments.

## Author contributions

RS is responsible for data curation, formal analysis, and writing the manuscript draft. WGP prepared the samples and provided resources for the experiments, AVK and EVP helped in the method and data analysis, CLC is responsible for funding acquisition, supervision, project administration, data analysis, manuscript writing, review, and editing.

## Conflicts of interest

The authors state that there are no conflicts of interest to declare.

## Acknowledgements

The authors would like to acknowledge the financial support by the National Science and Technology Council (NSTC) of Taiwan (NSTC-112-2112-M-259-010).

## References

1 E. Perevedentseva, Y. C. Lin and C. L. Cheng, *Expert Opin. Drug Delivery*, 2021, **18**, 369–382.
2 V. N. Mochalin, O. Shenderova, D. Ho and Y. Gogotsi, *Nat. Nanotechnol.*, 2012, **7**, 11–23.
3 F. F. Zhou, X. S. Li, S. Song, J. T. Acquaviva, R. F. Wolf, E. W. Howard and W. R. Chen, *J. Innovative Opt. Health Sci.*, 2013, **6**, 1350039.
4 P. D. Ray, B. W. Huang and Y. Tsuji, *Cell. Signal.*, 2012, **24**, 981–990.
5 P. T. Schumacker, *Cancer Cell*, 2015, **27**, 156–157.
6 B. D'Autreaux and M. B. Toledano, *Nat. Rev. Mol. Cell Biol.*, 2007, **8**, 813–824.
7 J. E. Moulder and S. Rockwell, *Cancer Metastasis Rev.*, 1987, **5**, 313–341.
8 S. Mallidi, S. Anbil, A. L. Bulin, G. Obaid, M. Ichikawa and T. Hasan, *Theranostics*, 2016, **6**, 2458–2487.
9 J. Kim, H. R. Cho, H. Jeon, D. Kim, C. Song, N. Lee, S. H. Choi and T. Hyeon, *J. Am. Chem. Soc.*, 2017, **139**, 10992–10995.
10 Z. J. Zhou, J. B. Song, R. Tian, Z. Yang, G. C. Yu, L. S. Lin, G. F. Zhang, W. P. Fan, F. W. Zhang, G. Niu, L. M. Nie and X. Y. Chen, *Angew. Chem., Int. Ed.*, 2017, **56**, 6492–6496.
11 P. P. Hsu and D. M. Sabatini, *Cell*, 2008, **134**, 703–707.
12 T. P. Szatrowski and C. F. Nathan, *Cancer Res.*, 1991, **51**, 794–798.
13 N. Aykin-Burns, I. M. Ahmad, Y. Zhu, L. W. Oberley and D. R. Spitz, *Biochem. J.*, 2009, **418**, 29–37.
14 D. Hanahan and R. A. Weinberg, *Cell*, 2011, **144**, 646–674.
15 K. M. Holmstrom and T. Finkel, *Nat. Rev. Mol. Cell Biol.*, 2014, **15**, 411–421.
16 R. C. Brewster, E. Klemencic and A. G. Jarvis, *J. Inorg. Biochem.*, 2021, **215**, 111317.
17 P. Das, S. Ganguly, T. Agarwal, P. Maity, S. Ghosh, S. Choudhary, S. Gangopadhyay, T. K. Maiti, S. Dhara, S. Banerjee and N. C. Das, *Mater. Chem. Phys.*, 2019, **237**, 121860.
18 H. Y. Xia, B. Y. Li, Y. T. Ye, S. B. Wang, A. Z. Chen and R. K. Kankala, *Adv. Healthcare Mater.*, 2023, e2303582, DOI: **10.1002/adhm.202303582**.
19 Y. Wang, Y. X. Liu and J. J. Xu, *Chem. Eng. J.*, 2019, **359**, 1486–1492.
20 N. Lewinski, V. Colvin and R. Drezek, *Small*, 2008, **4**, 26–49.
21 F. Mijangos, F. Varona and N. Villota, *Environ. Sci. Technol.*, 2006, **40**, 5538–5543.
22 K. Deng, C. Li, S. Huang, B. Xing, D. Jin, Q. Zeng, Z. Hou and J. Lin, *Small*, 2017, **13**, 1702299.
23 Z. M. Tang, Y. Y. Liu, M. Y. He and W. B. Bu, *Angew. Chem., Int. Ed.*, 2019, **58**, 946–956.
24 R. Ameta, A. K. Chohadia, A. Jain and P. B. Punjabi, in *Advanced Oxidation Processes for Waste Water Treatment*, 2018, pp. 49–87, DOI: **10.1016/b978-0-12-810499-6.00003-6**.
25 B. A. Wagner, C. B. Evig, K. J. Reszka, G. R. Buettner and C. P. Burns, *Arch. Biochem. Biophys.*, 2005, **440**, 181–190.
26 S. Patil, V. S. Mishra, P. C. Reddy and B. Lochab, *ACS Mater. Lett.*, 2023, **5**, 336–340.
27 B. R. Lin, C. H. Chen, S. Kunuku, T. Y. Chen, T. Y. Hsiao, H. Niu and C. P. Lee, *Sci. Rep.*, 2018, **8**, 7058.
28 S. Osswald, V. N. Mochalin, M. Havel, G. Yushin and Y. Gogotsi, *Phys. Rev. B: Condens. Matter Mater. Phys.*, 2009, **80**, 075419.
29 M. Hanesch, *Geophys. J. Int.*, 2009, **177**, 941–948.
30 O. N. Shebanova and P. Lazor, *J. Raman Spectrosc.*, 2003, **34**, 845–852.
31 T. Yamashita and P. Hayes, *Appl. Surf. Sci.*, 2009, **255**, 8194.
32 T. Fujii, F. M. F. de Groot, G. A. Sawatzky, F. C. Voogt, T. Hibma and K. Okada, *Phys. Rev. B: Condens. Matter Mater. Phys.*, 1999, **59**, 3195–3202.
33 A. C. Gandhi, R. Selvam, C. L. Cheng and S. Y. Wu, *Nanomaterials*, 2021, **11**, 648.
34 A. Bajorek, C. Berger, M. Dulski, M. Zubko, S. Lewinska, K. Prusik, A. Slawska-Waniewska, F. Grasset and N. Randrianantoandro, *Metall. Mater. Trans. A*, 2022, **53**, 1208–1230.
35 A. V. Samrot, C. S. Sahithya, J. Selvarani A, S. K. Purayil and P. Ponnaiah, *Curr. Res. Green Sustainable Chem.*, 2021, **4**, 100042.
36 A. I. Ahmed, S. Mandal, L. Gines, O. A. Williams and C. L. Cheng, *Carbon*, 2016, **110**, 438–442.
37 E. Perevedentseva, A. Karmenyan, Y. C. Lin, C. Y. Song, Z. R. Lin, A-I- Ahmed, C. C. Chang, S. Norina, V. Bessalova, N. Perov, O. Levinson, B. Zousman and C. L. Cheng, *J. Biomed. Opt.*, 2018, **23**, 091404.
38 K. Locharoenrat, *Artif. Cell Nanomed. Biotechnol.*, 2019, **47**, 4053–4058.
39 J. J. Yan, Y. Guo, A. Altawashi, B. Moosa, S. Lecommandoux and N. M. Khashab, *New J. Chem.*, 2012, **36**, 1479–1484.
40 E. Perevedentseva, S. F. Hong, K. J. Huang, I. T. Chiang, C. Y. Lee, Y. T. Tseng and C. L. Cheng, *J. Nanopart. Res.*, 2013, **15**, 1843.

41 W. G. Pearl, E. V. Perevedentseva, A. V. Karmenyan, V. A. Khanadeev, S. Y. Wu, Y. R. Ma, N. G. Khlebtsov and C. L. Cheng, *J. Biophot.*, 2022, **15**, e202100264.
42 R. Selvam, A. Gandhi, S.-C. Hung, A. V. Karmenyan, E. Perevedentseva, W.-C. Yeh, S.-Y. Wu, H.-H. Chang and C.-L. Cheng, *Diamond Relat. Mater.*, 2023, **139**, 110398.
43 R. Selvam, S. Ramasamy, S. Mohiyuddin, I. V. M. V. Enoch, P. Gopinath and D. Filimonov, *Mater. Sci. Eng., C*, 2018, **93**, 125–133.
44 B. A. Teicher, *Cancer Metastasis Rev.*, 1994, **13**, 139–168.
45 Y. L. Chen, T. Y. Yang, K. C. Chen, C. L. Wu, S. L. Hsu and C. M. Hsueh, *Cell. Oncol.*, 2016, **39**, 411–433.
46 Y. X. Sun, D. Y. Zhao, G. Wang, Y. Wang, L. L. Cao, J. Sun, Q. K. Jiang and Z. G. He, *Acta Pharm. Sin. B*, 2020, **10**, 1382–1396.
47 X. Zhang, C. He, Y. Chen, C. Chen, R. Yan, T. Fan, Y. Gai, T. Yang, Y. Lu and G. Xiang, *Biomaterials*, 2021, **275**, 120987.
48 M. Lopez-Lazaro, *Cancer Lett.*, 2007, **252**, 1–8.
49 Q. Wang, S. L. Tian and P. Ning, *Ind. Eng. Chem. Res.*, 2014, **53**, 643–649.
50 J. Z. Du, L. A. Lane and S. M. Nie, *J. Controlled Release*, 2015, **219**, 205–214.
51 B. C. Faust and J. Hoigne, *Atmos. Environ., Part A*, 1990, **24**, 79–89.
52 P. Kuppusamy, H. Q. Li, G. Ilangovan, A. J. Cardounel, J. L. Zweier, K. Yamada, M. C. Krishna and J. B. Mitchell, *Cancer Res.*, 2002, **62**, 307–312.
53 S. Wang, Z. T. Wang, G. C. Yu, Z. J. Zhou, O. Jacobson, Y. J. Liu, Y. Ma, F. W. Zhang, Z. Y. Chen and X. Y. Chen, *Adv. Sci.*, 2019, **6**, 1801986.
54 O. Tacar, P. Sriamornsak and C. R. Dass, *J. Pharm. Pharmacol.*, 2013, **65**, 157–170.
55 Y. Fu, M. S. Jang, C. L. Liu, Y. Li, J. H. Lee and H. Y. Yang, *ACS Appl. Mater. Interfaces*, 2023, **15**, 36013–36024.
56 J. Kim, H. R. Cho, H. Jeon, D. Kim, C. Song, N. Lee, S. H. Choi and T. Hyeon, *J. Am. Chem. Soc.*, 2017, **139**, 10992–10995.
57 E. Gottlieb, S. M. Armour, M. H. Harris and C. B. Thompson, *Cell Death Differ.*, 2003, **10**, 709–717.
58 S. Zhang, X. B. Liu, T. Bawa-Khalfe, L. S. Lu, Y. L. Lyu, L. F. Liu and E. T. H. Yeh, *Nat. Med.*, 2012, **18**, 1639–1642.
59 T. Simunek, M. Sterba, O. Popelova, M. Adamcova, R. Hrdina and V. Gersl, *Pharmacol. Rep.*, 2009, **61**, 154–171.
60 E. K. Chow, X. Q. Zhang, M. Chen, R. Lam, E. Robinson, H. Huang, D. Schaffer, E. Osawa, A. Goga and D. Ho, *Sci. Transl. Med.*, 2011, **3**, 73ra21.